Revealing the Various Electrochemical Behaviors of Sn_4P_3 Binary Alloy Anodes in Alkali Metal Ion Batteries

Junhua Zhou, Xueyu Lian, Yizhou You, Qitao Shi, Yu Liu, Xiaoqin Yang, Lijun Liu, Dan Wang, Jin-Ho Choi,* Jingyu Sun,* Ruizhi Yang,* and Mark H. Rummeli*

Sn_4P_3 binary alloy anode has attracted much attention, not only because of the synergistic effect of P and Sn, but also its universal popularity in alkali metal ion batteries (AIBs), including lithium-ion batteries (LIBs), sodium-ion batteries (SIBs), and potassium-ion batteries (PIBs). However, the alkali metal ion (A^+) storage and capacity attenuation mechanism of Sn_4P_3 anodes in AIBs are not well understood. Herein, a combination of ex situ X-ray diffraction, transmission electron microscopy, and density functional theory calculations reveals that the Sn_4P_3 anode undergoes segregation of Sn and P, followed by the intercalation of A^+ in P and then in Sn. In addition, differential electrochemical curves and ex situ XPS results demonstrate that the deep insertion of A^+ in P and Sn, especially in P, contributes to the reduction in capacity of AIBs. Serious sodium metal dendrite growth causes further reduction in the capacity of SIBs, while in PIBs it is the unstable solid electrolyte interphase and sluggish dynamics that lead to capacity decay. Not only the failure mechanism, including structural deterioration, unstable SEI, dendrite growth, and sluggish kinetics, but also the modification strategy and systematic analysis method provide theoretical guidance for the development of other alloy-based anode materials.

1. Introduction

Alkali metal ion batteries (AIBs), such as lithium-ion batteries (LIBs), sodium-ion batteries (SIBs), and potassium-ion batteries (PIBs), exhibit high working voltages, owing to the high electronegativity of alkali metals (A) and rapid kinetics on account of the monovalent alkali metal ions (A^+).[1–3]

Although LIBs have been successfully commercialized due to their high energy density, high operating voltage, and long cycle life, the limited lithium resources in the earth's crust restrict their further development.[4,5] Despite the usually lower energy density of SIBs and PIBs than LIBs, the rich resources and low cost of sodium and potassium give them certain marketability in special application fields.[6,7] In addition, sodium and potassium are in the same group in the periodic table as lithium, and thus some experience from work with LIBs, such as electrode materials, electrolytes, separators, and battery manufacturing technologies, can also be used for reference in the development of SIBs and PIBs.[8,9] AIBs all have their advantages and disadvantages, which can be employed in various scenarios. For instance, LIBs are usually utilized in consumer electronics and electric vehicles with high energy density requirements, and SIBs and PIBs may be used in large-scale energy storage grids that take cost into consideration.[8–11]

Energy density is one of the most crucial indices to evaluate a battery's performance. The energy density is mainly related to the electrode materials and the battery manufacturing process.[12] Although the carbon material with an intercalation mechanism is one the most popular anode materials in AIBs

J. Zhou, X. Lian, Y. You, Q. Shi, Y. Liu, D. Wang, Prof. J.-H. Choi,
Prof. J. Sun, Prof. R. Yang, Prof. M. H. Rummeli
College of Energy
Soochow Institute for Energy and Materials InnovationS (SIEMIS)
Key Laboratory of Advanced Carbon Materials and Wearable Energy
Technologies of Jiangsu Province
Soochow University
Suzhou 215006, P. R. China
E-mail: jhchoi@suda.edu.cn; sunjy86@suda.edu.cn; yangrz@suda.edu.cn;
mhr1@suda.edu.cn

X. Yang, Prof. L. Liu
School of Energy and Power Engineering
Xi'an Jiaotong University
No. 28, Xianning West Road, Xi'an, Shaanxi 710049, P. R. China

Prof. J. Sun
Beijing Graphene Institute (BGI)
Beijing 100095, P. R. China

Prof. M. H. Rummeli
Leibniz Institute for Solid State and Materials Research Dresden
P.O. Box 270116, D-01171 Dresden, Germany

Prof. M. H. Rummeli
Centre of Polymer and Carbon Materials
Polish Academy of Sciences
M. Curie-Sklodowskiej 34, Zabrze 41-819, Poland

Prof. M. H. Rummeli
Institute of Environmental Technology
VSB-Technical University of Ostrava
17. Listopadu 15, Ostrava 708 33, Czech Republic

(namely, graphite for LIBs and PIBs, and hard carbon for SIBs), their low specific capacity limits their energy density.[13,14] Phosphorus (P), with a multi-electron alloying mechanism, shows a high theoretical specific capacity in AIBs (2590 mAh g^{-1} for A_3P as the final discharge products).[3] However, the huge volume change (≈300% in LIBs and ≈400% in SIBs) and low conductivity (10^{-14} S cm^{-1} for red P and 0.2–3.3 S cm^{-1} for black P) restrict the cycling and rate performance of P in AIBs.[15] Contemporary modification strategies mainly include nanocrystallization, carbon coating, alloying, and functional electrolyte and binder exploration.[16–21] Alloying can not only enhance the bulk conductivity and buffer volume expansion of P, but also sometimes provide additional capacity depending on whether the second phase metal is participating in the formation of the alloy. Although the theoretical gravimetric capacities of tin (Sn) are lower than those for P, the volumetric capacities of Sn can compensate for this disadvantage, and the conductivity of Sn is better than that of P.[22–24] Based on this, many studies have been reported on P–Sn binary alloys that show excellent performances owing to the synergistic effect of P and Sn in AIBs.[22,25–27]

Although P–Sn alloys can store Li$^+$, Na$^+$, and K$^+$ separately, there is a notable difference in their electrochemical behaviors, such as the specific capacity, voltage platform, polarization voltage, Coulombic efficiency, cycling, and rate performance in various AIBs.[25,26] Comparing these disparities can be conducive to determine exactly what kind of alkali metal ion it best suits for storage.[3] However, very few studies have been

systematically conducted to explore and explain these diversities. Here, we use Sn_4P_3 as an example to detect the various electrochemical behaviors of Sn–P binary alloys in AIBs. The origin of the discrepancies in their electrochemical behaviors is then analyzed from the perspective of structural transformation, dynamics mechanism, solid electrolyte interface (SEI) evolution, alkali metal deposit, and density functional theory (DFT) calculations. Finally, we present our attempt to improve the capacity retention of Sn_4P_3 through carbon hybridization.

2. Results and Discussion

2.1. Physical and Electrochemical Characterization of Sn_4P_3

Sn_4P_3 was prepared by a facile mechanical ball milling method with stoichiometric P and Sn power, and its crystal structure, morphology, and electrochemical properties were obtained using X-ray diffraction (XRD), scanning electron microscopy (SEM), transmission electron microscopy (TEM), and 2032 coin cell tests. The XRD results (**Figure 1**d and Figure S1: Supporting Information) show that the synthesized material is pure Sn_4P_3 (hexagonal system, *R-3m* space group, PDF 73–1820) with a potato-like morphology and particle size of ≈3 µm (Figure 1a,b and Figure S2: Supporting Information). The lattice fringe in the high-resolution TEM (HRTEM) image (Figure 1c) can be indexed in the (107) plane, which is consistent with the strongest diffraction peak in the XRD pattern.
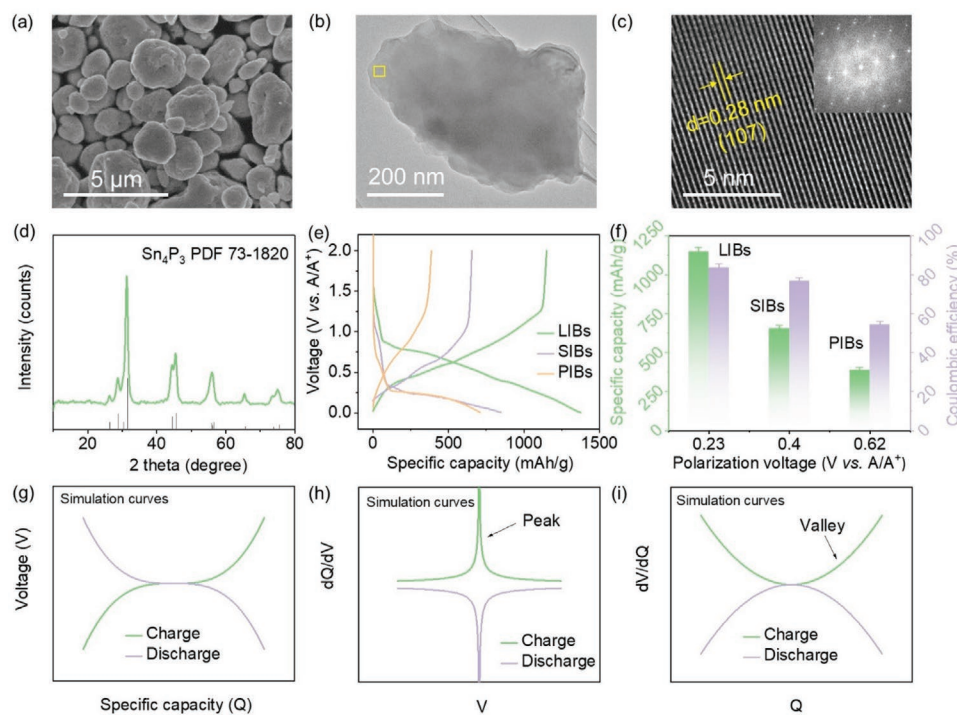
Figure 1. Physical and electrochemical characterization of Sn_4P_3. a,b) SEM (a) and TEM (b) images of Sn_4P_3. c) HRTEM image of selected area of (b). Inset: the corresponding FFT pattern. d) XRD spectrum with the standard PDF card of Sn_4P_3. e) Galvanostatic discharge–charge curves at 0.1 C (1 C = 1100 mA g^{-1} for LIBs, 1 C = 600 mA g^{-1} for SIBs, 1 C = 400 mA g^{-1} for PIBs) between 0.005 and 2 V for the Sn_4P_3 anode at the first cycle in AIBs. f) Statistical data with error bars of reversible specific capacity, Coulomb efficiency, and polarization voltage drawn from (e). All data in this paper was repeated at least three times and is shown with error bars if possible. g–i) Simulation discharge–charge (g), V versus dQ/dV (h), and Q versus dV/dQ (i) curves for better understanding of their respective roles.

The inclined discharge–charge curves (Figure 1e) indicate the multistep reaction mechanism of Sn_4P_3 in LIBs, delivering a large reversible specific capacity (1150 mAh g^{-1}), high Coulomb efficiency (87.2%), and low polarization voltage (0.23 V vs Li/Li$^+$) (Figure 1f and Figure S3: Supporting Information). In contrast, although Sn_4P_3 displays a low average sodiation voltage ($\approx$0.4 V vs Na/Na$^+$), which is related to the high formation energy of the discharge species in SIBs (Figure 3a), its flat reversible capacity (654 mAh g^{-1}), gentle Coulomb efficiency (80.1%), and large polarization (0.4 V vs Na/Na$^+$) will cancel out its low-potential advantage. As for PIBs, while their insertion plots are almost the same as those of SIBs, they demonstrate the worst reversible capacity (386 mAh g^{-1}), Coulomb efficiency (56.7%), and polarization voltage (0.62 V vs K/K$^+$) among all AIBs considered herein.

Differential discharge–charge patterns, mainly V versus dQ/dV and Q versus dV/dQ (where V and Q represent the voltage and capacity of a special electrode material), will be frequently used for exploring the reaction mechanism of Sn_4P_3 in this paper, and simulation curves (Figure 1g–i) are depicted here to better understand their respective roles in advance. It can be clearly seen that the platform in the discharge–charge curves, i.e., the phase transition process, is reflected in the form of a "peak" in

the V versus dQ/dV patterns, and in the form of a "Valley" in the Q versus dV/dQ curves. In addition, the V versus dQ/dV and Q versus dV/dQ patterns are mainly utilized to analyze the potential and capacity when the phase transition occurs, respectively (more details about the V versus dQ/dV and Q versus dV/dQ curves can be found in Figure S4, Supporting Information).

2.2. Structural Transformation of Sn_4P_3 Anodes during the Initial Cycle in AIBs

In order to reveal the origin of the various electrochemical behaviors for Sn_4P_3 anodes in AIBs, a combination of the V versus dQ/dV curves, ex situ XRD, and TEM techniques was explored to detect its structural evolution during the insertion–extraction process. (We failed to conduct in situ XRD tests owing to the low crystallinity of the P- and Sn-based species during electrochemical processes.) The V versus dQ/dV curves for the first cycle in LIBs exhibit four typical pairs of peaks, and each one corresponds to a redox process, labeled as Li1, Li2, Li3, and Li4 (**Figure 2**a). During the stage of the discharge from 2–0.83 V (vs Li/Li$^+$), the flat shape of the V versus dQ/dV curve and the absence of an updated Bragg peak at 0.83 V compared with the initial XRD
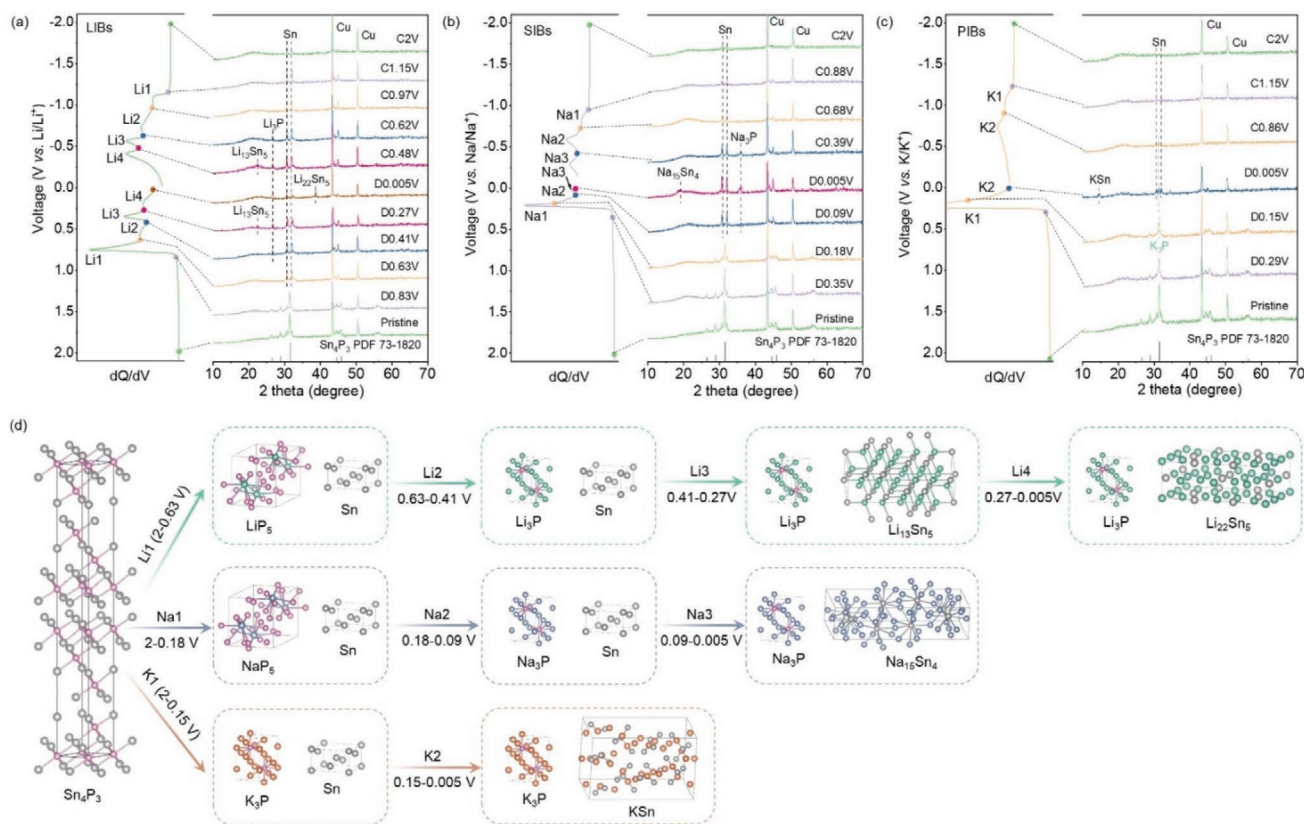
Figure 2. Structural transformation of Sn_4P_3 anodes in AIBs. a–c) V versus dQ/dV curves for detecting the position at which phase transformation occurs and the corresponding ex situ XRD plots for determining the specific species formed in these positions of Sn_4P_3 cycled at various states in LIBs (a), SIBs (b), and PIBs (c). d) Schematic diagram of the discharge mechanism based on (a–c) for the Sn_4P_3 anode in AIBs. The Sn_4P_3 anode exhibits various ion storage mechanisms in AIBs, delivering four (labeled as Li1, Li2, Li3, and Li4), three (labeled as Na1, Na2, and Na3) and two steps (labeled as K1 and K2) in LIBs, SIBs and PIBs, respectively. Pink, grey, cyan, dark blue, and dark yellow balls represent the P, Sn, Li, Na, and K atoms, respectively.

pattern demonstrate that it belongs to the Ohmic voltage-drop process. With continued discharge to 0.63 V, all diffraction peaks belong to Sn (PDF 86–2265), except that of the Cu current collector, indicating the decomposition of Sn_4P_3 into metallic Sn and amorphous low lithiation phosphides (such as LiP_7, LiP_5, Li_3P_7, and LiP) during the Li1 process (0.83–0.63 V). In fact, the existence of Sn is detectable in the entire intercalation–deintercalation process, resulting in better conductivity, unless damage occurs from losing partial capacity. Fresh Bragg peaks with low crystallinity at 0.41 V could be indexed to Li_3P (PDF 74–1160), demonstrating the conversion from an amorphous low lithiation phosphide to Li_3P during the Li2 process (0.63–0.41 V). Thereafter, at 0.27 V new XRD peaks cannot be determined exclusively, owing to the similar standard diffraction peaks of the low lithiation stannide species, including Li_5Sn_2 (PDF 29–0839), $Li_{13}Sn_5$ (PDF 29–0838), and Li_7Sn_2 (PDF 29–0837) (Table S1, Supporting Information). Thus the Li3 process (0.41–0.27 V) represents the transformation from Sn to low lithiation stannide compounds. The complete lithiation species could be attributed to Li_3P and $Li_{22}Sn_5$ (PDF 18–0753), based on the diffraction peaks at 0.005 V, revealing the conversion from low lithiation stannide to $Li_{22}Sn_5$ (Li4 process, 0.27–0.005 V). The subsequent delithiation process is an almost complete reverse of the lithiation process, since the resulting compounds are made up of Sn nanocrystalline surrounded by an amorphous P matrix rather than Sn_4P_3, as evidenced by using combined characterization of ex situ XRD and HRTEM at 2 V (Figure S5, Supporting Information).

Analogical analysis methods have also been applied to the Sn_4P_3 anodes in SIBs and PIBs (Figure 2b,c), and their reaction mechanism has been determined using the following equation together with Figure 2d.

The lithiation mechanism (four steps) of Sn_4P_3 is:

Li1: Sn_4P_3 +Li→ Sn + low lithiation phosphide {LiP_7, LiP_5, Li_3P_7, LiP} (shallow lithiation of P)
Li2: Sn + low lithiation phosphide {LiP_7, LiP_5, Li_3P_7, LiP} +Li→ Sn + Li_3P (deep lithiation of P)
Li3: Sn + Li_3P +Li→ low lithiation stannide {Li_5Sn_2, $Li_{13}Sn_5$, Li_7Sn_2} + Li_3P (shallow lithiation of Sn)
Li4: low lithiation stannide {Li_5Sn_2, $Li_{13}Sn_5$, Li_7Sn_2} + Li_3P+Li → $Li_{22}Sn_5$ + Li_3P (deep lithiation of Sn)

The sodiation mechanism (three steps) of Sn_4P_3 is:

Na1: Sn_4P_3 +Na → Sn + low sodiation phosphide {NaP_5, Na_3P_{11}, NaP} (shallow sodiation of P)
Na2: Sn + low sodiation phosphide {NaP_5, Na_3P_{11}, NaP} +Na → Sn + Na_3P (deep lithiation of P)
Na3: Sn + Na_3P +Na→ $Na_{15}Sn_4$ + Na_3P (sodiation of Sn)

The potassiation mechanism (two steps) of Sn_4P_3 is:

K1: Sn_4P_3 +K→ Sn + K_3P (potassiation of P)
K2: Sn + K_3P +K → KSn + K_3P (potassiation of Sn)

Overall, Sn_4P_3 undergoes segregation of Sn and P, and then A^+ reacts with P and finally with Sn during the intercalation process. However, the number of phase transition stages varies in AIBs (Li1, Li2, 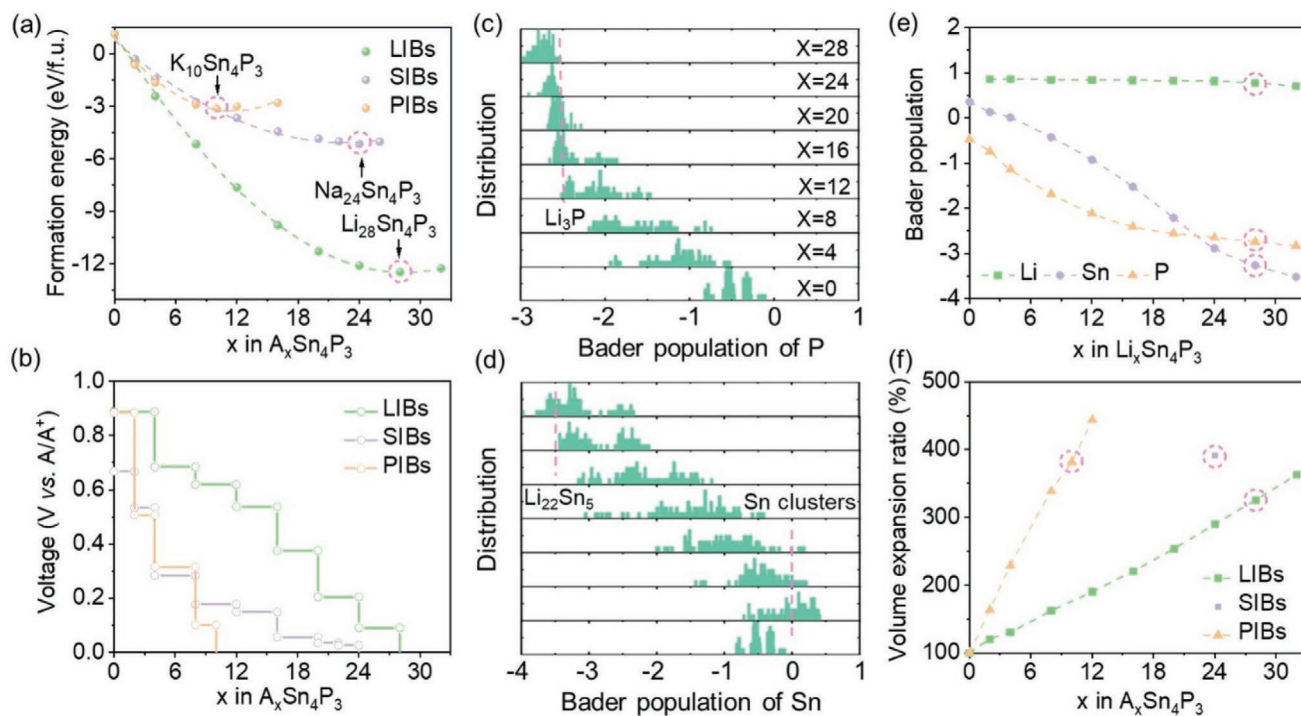Li3, and Li4 for LIBs; Na1, Na2, and Na3 for SIBs; K1 and K2 for PIBs), depending on whether P or Sn are involved in the shallow intercalation process. Furthermore, the ultimate discharge species of Sn_4P_3 anodes are $Li_{22}Sn_5$, Li_3P, $Na_{15}Sn_4$ (PDF 31–1327), Na_3P (PDF 04–0764), KSn (PDF 65–7670), and K_3P (PDF 74–0128), with the corresponding theoretical specific capacities of 1256, 1133, and 613 mAh g^{-1} in LIBs, SIBs, and PIBs, respectively. In fact, the element P in the Sn_4P_3 compound will always be converted to A_3P after the complete discharge process in all three kinds of AIBs, and thus, the varied theoretical capacities are mainly attributed to the diverse Sn-based species, i.e., $Li_{22}Sn_5$ for LIBs, $Na_{15}Sn_4$ for SIBs, and KSn for PIBs.

2.3. DFT Calculations of Sn_4P_3 Anodes in AIBs

To further demonstrate the alkali metal ion storage mechanism of Sn_4P_3 anodes in AIBs, we performed DFT calculations for $A_xSn_4P_3$ with amorphous structural models, considering the pulverization of Sn_4P_3 during the charge–discharge reactions (see the Methods section).[26,28] The calculated formation energy curves exhibit minimum values at x = 28.29, 23.95, and 10.03 (**Figure 3**a) with corresponding theoretical specific capacities of 1335, 1131, and 473 mAh g^{-1} for A = Li, Na, and K, respectively, which agrees well with our experimental values. The calculated voltage profiles are also consistent with the experimental measurements (Figure 3b). The wide Bader charge distribution of P and Sn atoms in Figure 3c,d further demonstrates the coexistence of various Li–Sn and Li–P alloys during the entire alkali metal ion intercalation process. Some neutrally charged Sn atoms at x = 4 are located within Sn clusters, implying the segregation of Sn and P, consistent with our ex situ TEM measurements (Figure S5, Supporting Information). In addition, P atoms when $x \geq 12$ and Sn atoms at x = 28 deliver the majority of Bader charges of ≈–2.5 e and –3.4 e, giving evidence for the initial formation of Li_3P followed by $Li_{22}Sn_5$ (close to $Li_{28}Sn_4P_3$), validating the ex situ XRD observation.[29] The distribution histograms for PIBs (Figure S6, Supporting Information) also reveal that KSn and K_3P are formed (totally, close to $K_{10}Sn_4P_3$). A previous paper published by our collaborator demonstrated that the final discharge products in SIBs are $Na_{15}Sn_4$ and Na_3P (close to $Na_{24}Sn_4P_3$).[30] In Figure 3e the decreasing average Bader populations of Sn and P indicate the gradual reduction in these species and that P is more quickly saturated than Sn. In addition, the volumes of all the $A_xSn_4P_3$ increase almost linearly with increasing x, whereas the slope depends on the type of alkali metal (Figure 3f). Specifically, the calculated maximum volume expansions are ≈326%, 391%, and 382% for $Li_{28}Sn_4P_3$, $Na_{24}Sn_4P_3$, and $K_{10}Sn_4P_3$, respectively, resulting in restricted insertion processes of A^+, especially for Na^+ and K^+.

2.4. Capacity Decay Analysis of Sn_4P_3 Anodes in AIBs

In addition to the initial reversible specific capacity, the cycling performance is also a crucial index for estimating a battery's performance. The disparate cycling behaviors of Sn_4P_3 in AIBs are explored using Q versus dV/dQ curves to clarify the capacity contribution of each phase transition mentioned

**ADVANCED
SCIENCE NEWS**

www.advancedsciencenews.com

**ADVANCED
FUNCTIONAL
MATERIALS**

www.afm-journal.de

Figure 3. DFT calculation of Sn_4P_3 anodes in AIBs. a) The formation energy of $A_xSn_4P_3$. The final intercalation products which exhibit the lowest formation energy marked with pink circles are $Li_{28}Sn_4P_3$, $Na_{24}Sn_4P_3$, and $K_{10}Sn_4P_3$ in LIBs, SIBs, and PIBs, respectively. b) Average voltage profiles of $A_xSn_4P_3$ based on the formation energy in Figure (a). c,d) Bader charge distribution histograms of P (c) and Sn (d) in $Li_xSn_4P_3$. Bader charges of ≈ -2.5 e for P, -3.4 e for Sn, and 0 e for Sn (marked with pink lines) represent Li_3P, $Li_{22}Sn_5$, and Sn clusters, respectively. e) The average Bader charge population of Sn and P atoms drawn from (c) and (d). The charges marked with pink circles represent $Li_{28}Sn_4P_3$. f) The volume expansion plots of LIBs, SIBs, and PIBs. The volume expansions marked with pink circles represent $Li_{28}Sn_4P_3$, $Na_{24}Sn_4P_3$, and $K_{10}Sn_4P_3$ in LIBs, SIBs, and PIBs, respectively.

above. The Sn_4P_3 anode in LIBs presents an inferior cycling performance, with a capacity retention of $\approx 65.4\%$ (700 mAh g^{-1}) compared with the initial capacity (1070 mAh g^{-1}), and a Coulombic efficiency of $\approx 99.2\%$ after 50 cycles (**Figure 4**a). The shape of the corresponding discharge–charge curves at the 1st, 20th, and 50th cycles did not obviously change except for a gradually increasing polarization (Figure 4a, inset figure). Four valleys in the Q versus dV/dQ curves derived from the relevant charge curves reveal a four-step lithiation–delithiation mechanism for Sn_4P_3, in agreement with the result in Figure 2a, i.e., Li4→Li3→Li2→Li1 (representing the delithiation process, as shown in Figure 4d. It was found that the specific capacities attributed to the Li1 and Li3 phase transformations first increase and then decrease, while those resulting from the Li2 and Li4 processes decline continuously, indicating that the capacity decay in LIBs is mainly caused by the Li2 and Li4 stages, namely, the deep lithiation of P and Sn (Figure 4g). This is reasonable because the deep charge or discharge process usually results in huge volume changes, especially for alloy anodes,[31,32] as well as sluggish dynamics (Figure 7g) as discussed in the later section "Dynamics of Sn_4P_3 anode in AIBs".

For SIBs, the Sn_4P_3 anode exhibits a general cycling stability with a capacity retention of 78.2% (485 mAh g^{-1}) but poor Coulombic efficiency of 97.4% after 50 cycles (Figure 4b). The relevant charge–discharge curves at the 1st and 20th cycles almost coincide, whereas that of the 50th cycle changes greatly, with

the appearance of a more obvious charging platform at a low potential (Figure 4b, inset figure). Three valleys can be detected during the desodiation processes (Na3→Na2→Na1) at the 1st and 20th cycles, while the Na2 and Na1 stages merge (Na1+Na2) in the 50th cycle, demonstrating the combination of shallow and deep sodiation of the P stage (Figure 4e). The statistical data in Figure 4h show that the specific capacity of the Na3 stage is almost constant throughout the entire cycling process, implying that the fading of capacity during the last 30 cycles is mainly attributed to the sodiation of P (Na1+Na2) rather than Sn (Na3). This is due to the sluggish dynamics of P compared with Sn during the insertion–extraction reaction. With respect to PIBs, the "dive" phenomenon (a sudden drop in capacity) emerges at approximately the 15th cycle with a very low Coulomb efficiency of 81.7% (Figure 4c), indicating its pessimal electrochemical performance among AIBs. The shape of the corresponding charge–discharge curves changed sharply, with almost no capacity at the 50th cycle (Figure 4c, inset figure), resulting from the potassiation of both P and Sn (Figure 4i).

2.5. SEI Evolution of Sn_4P_3 Anodes in AIBs

Aside from the evolution of the bulk structure, the transformation of SEI also has a valuable impact on batteries' performance. HRTEM images reveal that the typical thickness of SEI
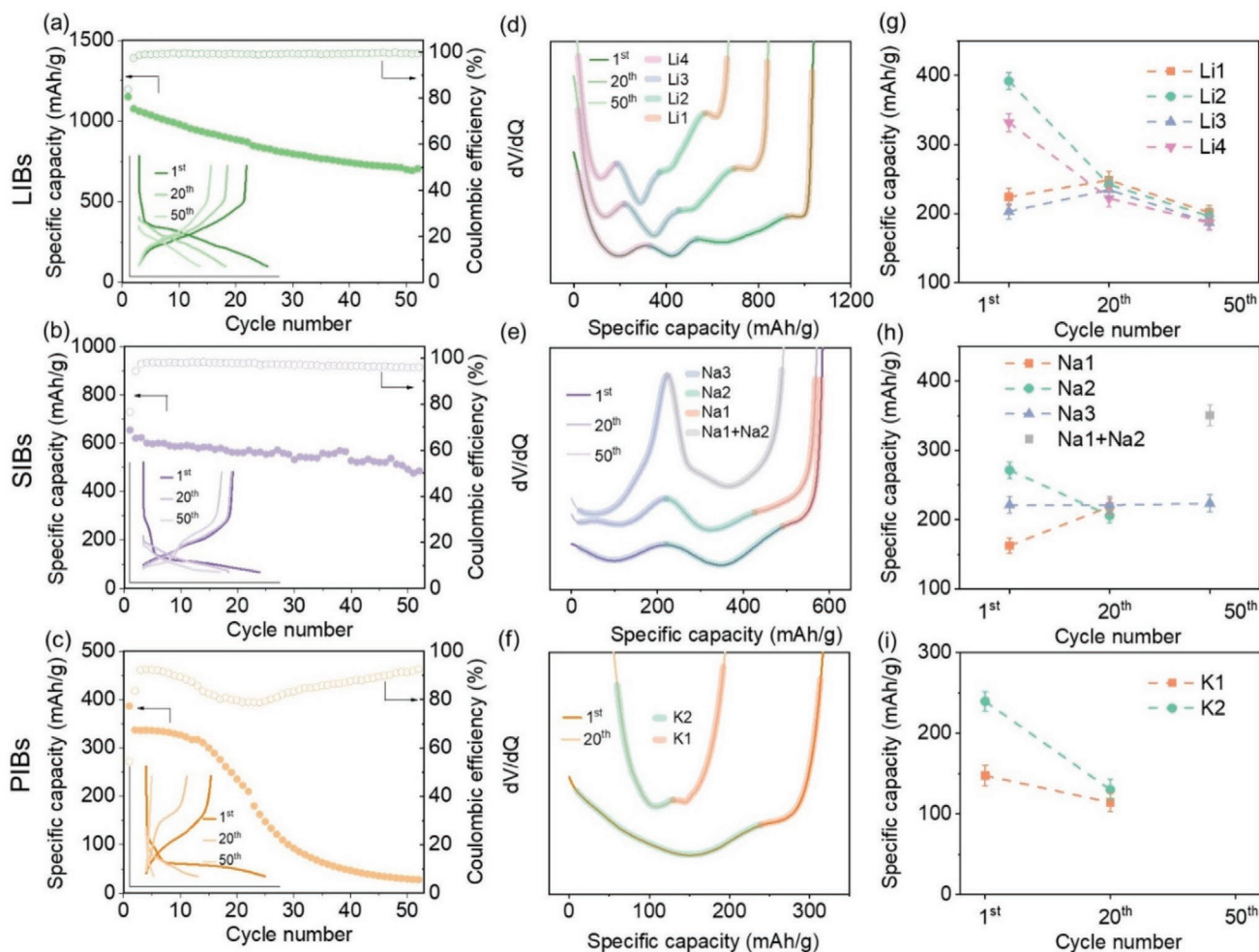
Figure 4. Capacity decay analysis of Sn_4P_3 anodes in AIBs. a–c) Reversible specific capacity, Coulombic efficiency, and corresponding galvanostatic discharge–charge curves (as inset) of Sn_4P_3 at 0.5 C in LIBs (a), SIBs (b), and PIBs (c). d–f) Q versus dV/dQ curves drawn from the galvanostatic discharge–charge curves in LIBs (d), SIBs (e), and PIBs (f). The lithiation, sodiation, and potassiation multistep intermediate reactions of the Sn_4P_3 process (which have been exhibited in Figure 2 and the capacity contribution of each step correspond with the valleys marked with various colors. g–i) Capacity decay analysis of Sn_4P_3 based on the data calculated from (d–f) in LIBs (g), SIBs (h), and PIBs (i).

for Sn_4P_3 anodes after 50 cycles in LIBs, SIBs, and PIBs are 9, 6, and 14 nm, respectively (**Figure 5**a–c, with additional images shown in Figure S10: Supporting Information). The SEM image (Figure S11, Supporting Information), EDS mapping (Figure S12, Supporting Information), and weakest Sn 3d XPS signal (Figure S13, Supporting Information) confirm that PIBs have the largest SEI thickness, because Sn_4P_3 particles coated with the thick SEI reduce the intensity of XPS signal. The decreasing Sn 3d XPS signature in LIBs indicates the thickening of the SEI during cycling, while the increasing Sn 3d XPS intensity in PIBs demonstrates that a cracked SEI exposes the fresh surface of the Sn_4P_3 electrode. The C 1s XPS spectra after cycling suggest that the composition of SEI in AIBs mainly incorporates carbon species, including CH_2–CF_2 ($\approx$290.2 eV), C=O ($\approx$288.8 eV), C–O ($\approx$286.5 eV), C–C/C–H ($\approx$285 eV), and RA (R = alkyl, $\approx$283 eV) (Figure 5d–f and Figure S14, Table S2: Supporting Information). These carbon species are primarily decomposed by electrolytes, such as salts ($LiPF_6$, $NaPF_6$, or KPF_6), carbonate solvents (ethylene carbonate (EC)

and dimethyl carbonate (DMC)), and additives (fluoroethylene carbonate (FEC)).[33,34] In addition, the polycarbonates (poly (CO_3), $\approx$291 eV) generated in LIBs and SIBs after 50 cycles by the Lewis reaction between PF_5 (Lewis acid, $APF_6 \rightarrow AF + PF_5$) and EC (monomer) could enhance the flexibility of the SEI, which is significant for an electrode with huge volume expansion.[33] However, no signal indexed to poly (CO_3) could be detected in PIBs during the initial 50 cycles, contributing to PIBs having the most unstable SEI character.

2.6. Alkali Metal Deposition Characteristics on Cu and Sn_4P_3 Anodes

A combination of the A–Cu battery test and the XPS spectra revealed that the various alkali metal ion deposition characteristics are another significant factor contributing to the diverse electrochemical behaviors of Sn_4P_3 anodes in AIBs. SEM images (**Figure 6**a–c) and the inset digital photographs reveal
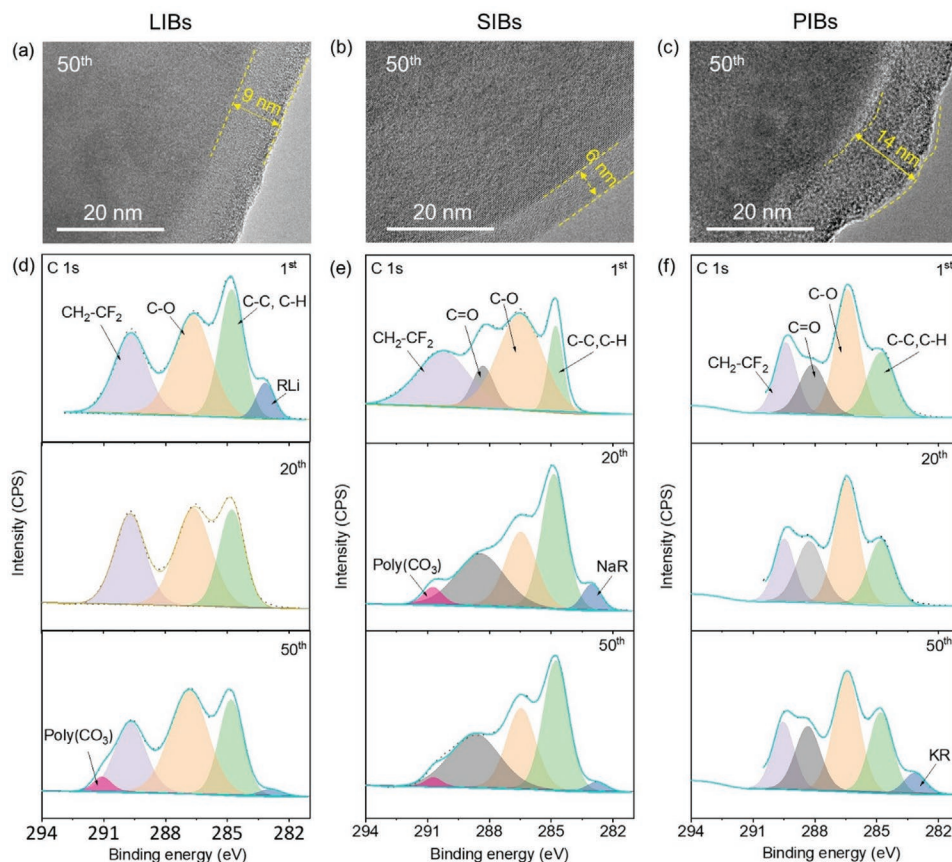
Figure 5. SEI evolution of Sn_4P_3 anode in AIBs. a–c) TEM images of Sn_4P_3 anodes after 50 cycles in LIBs (a), SIBs (b), and PIBs (c). d–f) C 1s XPS spectra of Sn_4P_3 anodes at the 1st, 20th, and 50th cycle in LIBs (d), SIBs (e), and PIBs (f).

the abundance of potassium metal dendrites with a columnar morphology (purple color) on Cu foil after 10 cycles in the K–Cu battery, and the corresponding sodium metal dendrite exhibits a moss-like morphology (silver color) in the Na–Cu battery (Figure 6b,c and Figure S17: Supporting Information). However, only the SEI with black color coating on carbon fibers coming from the separator could be observed in the Li–Cu battery (Figure 6a and Figure S17: Supporting Information). Further electrochemical tests demonstrate that the relatively low overpotential, high Coulombic efficiency, and minor impedance of the Li–Cu battery is ≈14 mV, 95.7%, and 152 Ω, respectively, and that for the Na–Cu battery is ≈20 mV, 80.5%, and 174 Ω, respectively (Figure 6a–c and Figures S17 and S18: Supporting Information). However, both the K–K battery (Figure S16, Supporting Information) and the K–Cu battery depict a marked overpotential, very low Coulombic efficiency, and pronounced impedance character. Moreover, the Li 1s, Na 1s, and K 2p XPS spectra of the Sn_4P_3 anode at the 1st, 20th, and 50th cycles represent the typical SEI species, including LiF (≈55.7 eV), NaF (≈1072.7 eV), and KF (2p1/2, ≈295 eV), mainly formed by the decomposition of FEC and APF_6 (Figure 6g–i).[35–37] In addition, Sn_4P_3 anodes in SIBs present a distinct peak shift, indicating the formation of sodium metal dendrites (≈1071 eV). This formation contributes to the relatively low sodium plating overpotential (20 mV) in Na–Cu battery and low discharge voltage platform of Sn_4P_3 anodes in SIBs (≈0.2 V vs Na/Na+).

2.7. Dynamics of Sn_4P_3 Anodes in AIBs

Finally, the effect of kinetic factors on the performance of Sn_4P_3 anode in AIBs was investigated using cyclic voltammetry (CV), galvanostatic intermittent titration technique (GITT), electrochemical impedance spectroscopy (EIS), and C-rate techniques. CV curves with variable scanning speeds from 0.2–2 mV s^{-1} between 0.005 and 2 V (vs A/A$^+$) reveal increasing polarization with increasing speed. This means that the oxidation peaks and reduction peaks shift in the positive and negative directions, respectively, in AIBs (**Figure 7**a–c). The minimum polarization voltage, maximum peak current density (10 A g^{-1} at 2 mV s^{-1}), and symmetric oxidation–reduction peaks of Sn_4P_3 in LIBs demonstrate their optimum dynamics in lithiation–delithiation systems. In addition, the charge storage mechanism can be determined from the relationship between the scanning speed (v) and the peak current (i) driven by the CV curves. This relationship is expressed as $i = av^b$, where a and b are the slope and y-intercept, respectively, in the $\lg(v)$ versus $\lg(i)$ curves (Figure 7d). The situations where $b = 0.5$ and $b = 1$ indicate that the system is controlled by bulk phase diffusion and surface capacitance, respectively. The contributions of these two mechanisms can be further separated by the relationship $i = k_1 v + k_2 v^{1/2}$ (k_1 and k_2 are the ratio for contributions of surface capacitance and bulk phase diffusion respectively) when b is between 0.5 and 1.[38] The supreme b value (0.97) and capacitance
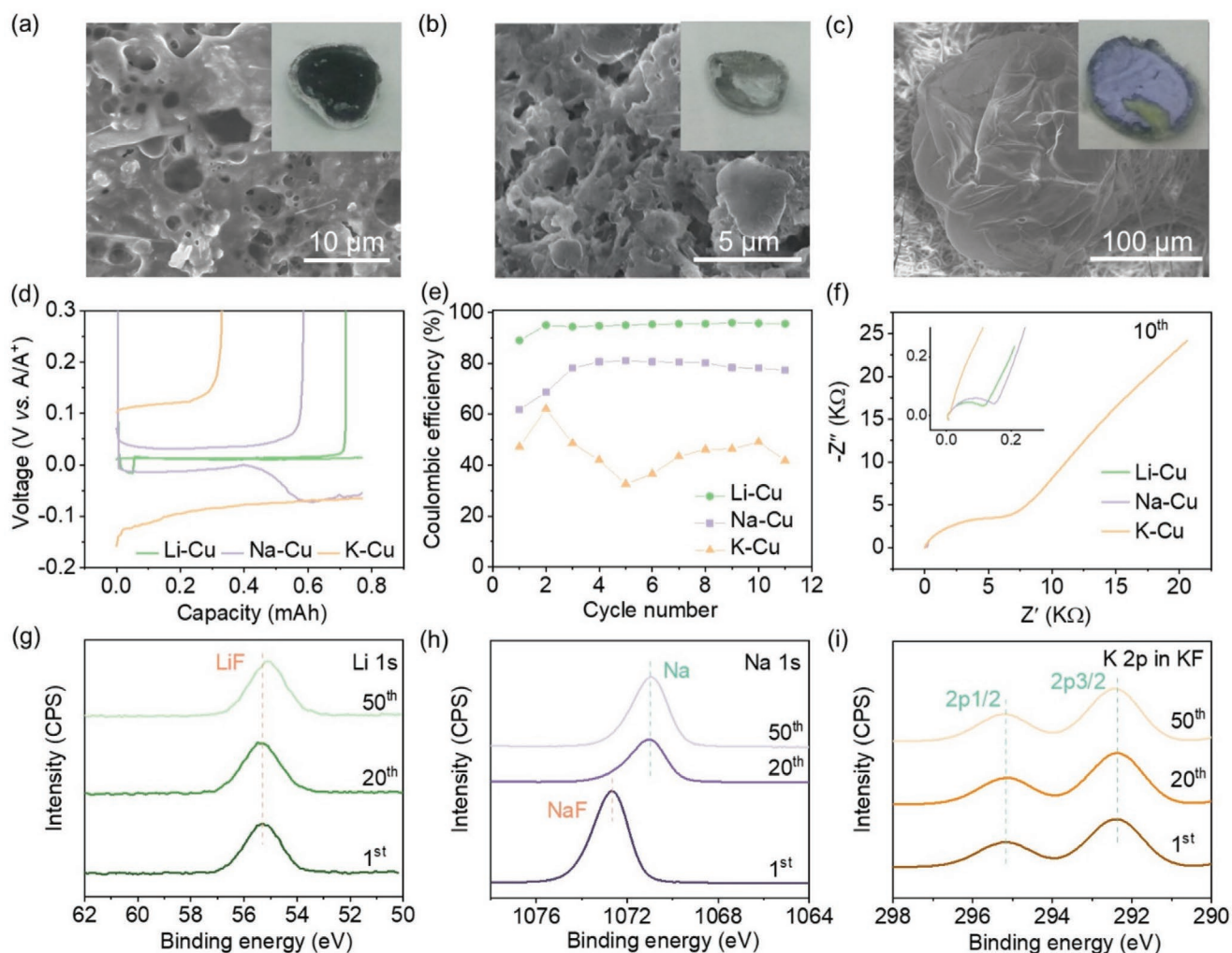
Figure 6. Alkali metal deposition characteristics on Cu and Sn_4P_3 anodes. a–c) Morphology of Li (a), Na (b), and K (c) metal plating on Cu foil after 10 cycles at a charged state. Inset: digital photographs of the separator close to the Cu foil. d–f) The discharge–charge curves at the 2nd cycle (d), Coulombic efficiencies (e), and corresponding EIS spectra (f) of Li–Cu, Na–Cu, and K–Cu battery cycled with the discharge capacity limit of 1 mAh cm^{-2} at 0.5 mA cm^{-2}. g–i) Li 1s (g), Na 1s (h), and K 2p (i) XPS spectra of Sn_4P_3 anodes at 1st, 20th, and 50th cycle in LIBs, SIBs, and PIBs.

contribution (the shaded area in Figure 7e of Sn_4P_3 in LIBs for all scan rates (Figure 7f) emphasize its mainly capacitance-controlled mechanism, resulting in its optimal rate performance (Figure 7i and Figure S20: Supporting Information). The ion diffusion coefficient (D) in the solid electrode, which is the rate-determining step (RDS), can be further examined using GITT (see details in Figure S19, Supporting Information). The D values in AIBs all exhibit a downward trend with an increase in the state of charge (SOC) (Figure 7i), indicating the constrained kinetic processes when alkali metal ions are deeply embedded in the Sn_4P_3 anode, consistent with the above results in the capacity decay analysis section. For various SOC values, both the minimum potassium ion diffusion coefficient, due to the largest ionic radius of K$^+$ among A$^+$ (0.076 nm for Li$^+$, 0.102 nm for Na$^+$, and 0.138 nm for K$^+$)[8], and the marked charge impedance (R_{ct}, Figure 7h and Figure S21: Supporting Information) reveal the sluggish dynamics of Sn_4P_3 anodes in PIBs.

2.8. Improving the Capacity Retention of Sn_4P_3 Anodes in SIBs through Carbon Hybridization

According to the electrochemical test mentioned above, Sn_4P_3 anode exhibits the lowest average voltage, best cycling performance, modest specific capacity and coulombic efficiency in SIBs among the explored AIBs, indicating its considerable application potential for sodium ion storage. Sn_4P_3/C (Figure S22, Supporting Information) was further synthesized using the flexible ball milling method to verify the role of carbon hybridization in improving the performance of the Sn_4P_3 anode in SIBs previously. Pure Sn_4P_3 shows the "diving" phenomenon after 50 cycles, whereas Sn_4P_3/C delivers a much better capacity retention of ≈80.9% after 180 cycles and a more stable Coulomb efficiency, in spite of having a relatively low initial specific capacity of 457 mAh g^{-1} resulting from the introduction of carbon materials with low capacity (**Figure 8**a,b and Figure S23: Supporting Information). Based on the charge
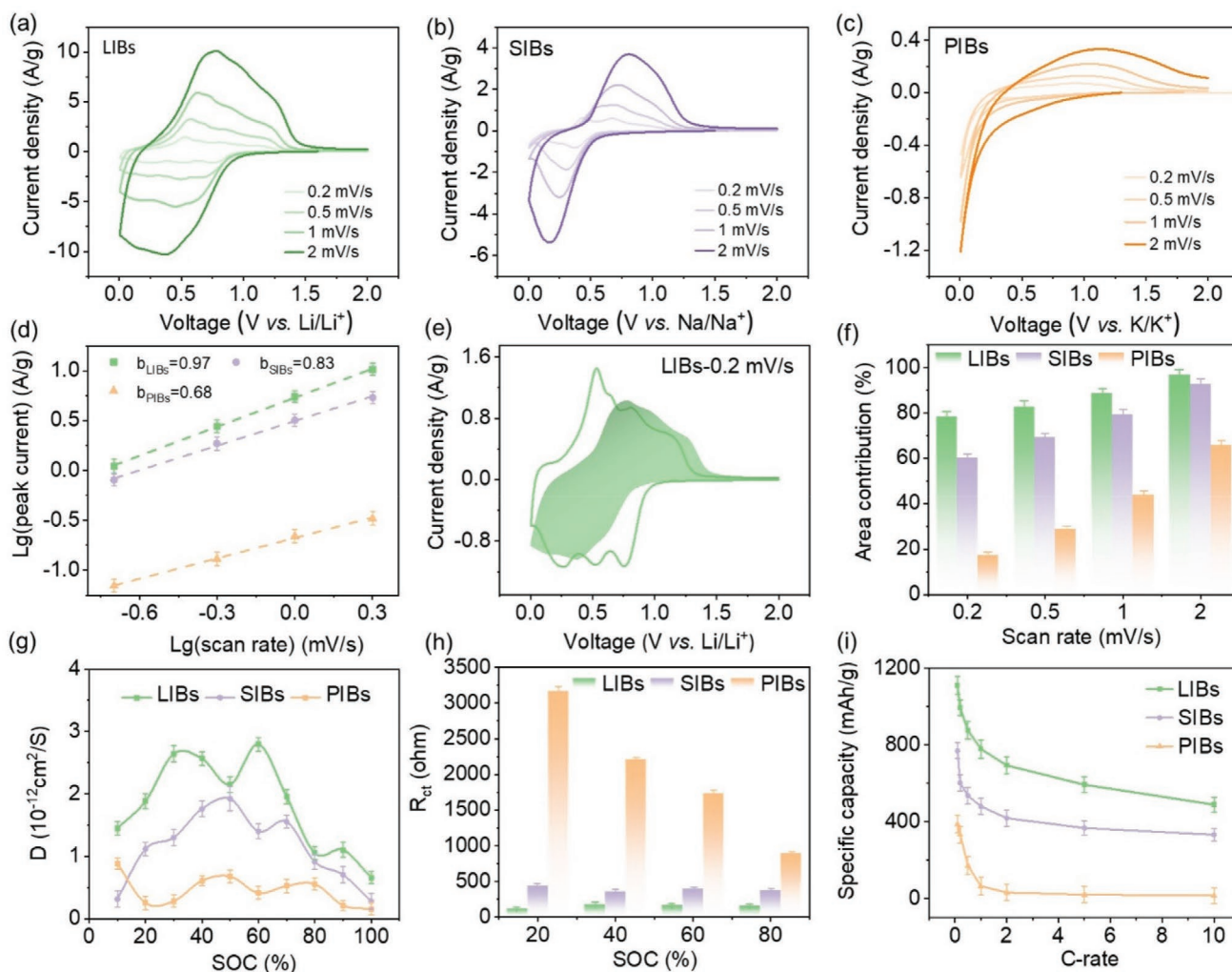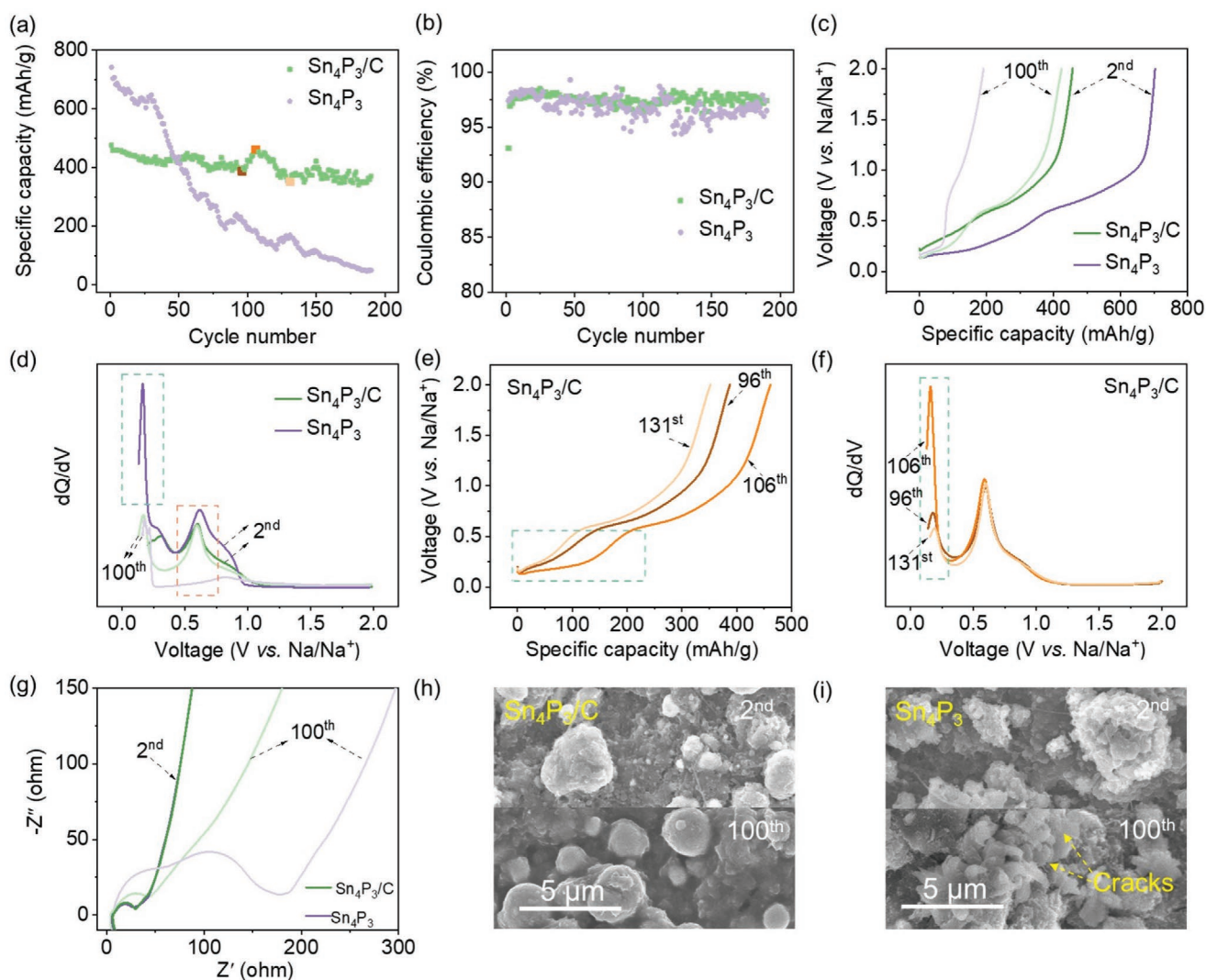
Figure 7. Dynamics of Sn_4P_3 anodes in AIBs. a–c) CV curves of Sn_4P_3 at 0.2, 0.5, 1, and 2 mV s^{-1} in LIBs (a), SIBs (b), and PIBs (c). d) Calculated *b*-values, based on the peak current and scan rates in (a–c). e) Separation of the capacitive (dashed area) and diffusion contribution of Sn_4P_3 at 0.2 mV s^{-1} in LIBs. f) Pseudocapacitive contribution comparison of Sn_4P_3 at various scan rates. g) Li$^+$, Na$^+$, and K$^+$ diffusion coefficients of Sn_4P_3 at diverse SOC values measured by GITT. h) Charge transfer impedances (R_{ct}) of Sn_4P_3 at varying SOC values. i) Rate performance of Sn_4P_3 from 0.1 C to 10 C.

curves (Figure 8c) and corresponding *V* versus d*Q*/d*V* plots (Figure 8d) at the 2nd and 100th cycles, both the P and Sn sodiation processes (shown by the dark yellow and blue rectangles, respectively) contribute to the fast capacity-fading of the pure Sn_4P_3 anode in SIBs, while these two processes present much more stable characteristics for the Sn_4P_3/C anode. Notably, the activation phenomenon marked by yellow dots in Figure 8a enhances the capacity retention of the Sn_4P_3/C anode, which is primarily caused by the extension of the platform at low potential (Figure 8e,f, blue rectangle) in the 96th and 106th cycles. Nevertheless, the subsequent capacity-fading at the 131st cycle indicates the fluctuating capacity characteristics due to the facile production of dendrites at low voltages for Sn_4P_3 in SIBs, which has been demonstrated in "Alkali metal deposition characteristics on Cu and Sn_4P_3 anodes" section. In addition, EIS tests (Figure 8g) depict a tiny mid-frequency impedance, even after 100 cycles for the Sn_4P_3/C anode, whereas this increases sharply for the pure Sn_4P_3 anode, revealing that the carbon

coating strategy can boost the electrical conductivity. Morphological evolution experiments further show severe particle pulverization in the pure Sn_4P_3 electrode (Figure 8i), owing to its large volume expansion during the extraction–insertion process of Na$^+$, while its structural integrity can be greatly improved through carbon hybridization (Figure 8h).

3. Conclusions

Using a combination of ex situ XRD, TEM, and DFT calculations, we demonstrate that the Sn_4P_3 anode initially undergoes segregation of Sn and P, followed by the intercalation of A$^+$ in P and then in Sn during the initial discharge processes. The various specific capacities of Sn_4P_3 anodes in AIBs are mainly attributed to the disparate number of phase transitions and ultimate insertion species ($Li_{22}Sn_5$ and Li_3P for LIBs; $Na_{15}Sn_4$ and Na_3P for SIBs; and KSn and K_3P for PIBs) (**Scheme** 1a).

**ADVANCED
SCIENCE NEWS**

www.advancedsciencenews.com

**ADVANCED
FUNCTIONAL
MATERIALS**

www.afm-journal.de

Figure 8. Improving the capacity retention of Sn_4P_3 anodes through carbon hybridization in SIBs. a,b) Reversible specific capacity (a) and Coulomb efficiency (b) of Sn_4P_3/C and Sn_4P_3 at 0.5 C (1 C = 600 mA g^{-1} for Sn_4P_3, 1 C = 500 mA g^{-1} for Sn_4P_3/C) during 180 cycles. c,d) Charge curves (c) and corresponding V versus dQ/dV plots (d) of Sn_4P_3/C and Sn_4P_3 at the 2nd and 100th cycle. The sodiation processes at a relatively high potential, attributed to P, and at a low potential, resulting from Sn, are labeled with a dark yellow and blue rectangle, respectively. e,f) Charge curves (e) and corresponding V versus dQ/dV plots (f) of Sn_4P_3/C at the 96th, 106th, and 131st cycle. These special cycles are marked in (a) for capacity activation analysis. g) Nyquist patterns of Sn_4P_3/C and Sn_4P_3 at the 2nd and 100th cycle. h,i) SEM images of Sn_4P_3/C (h) and Sn_4P_3 (i) at the 2nd and 100th cycle.
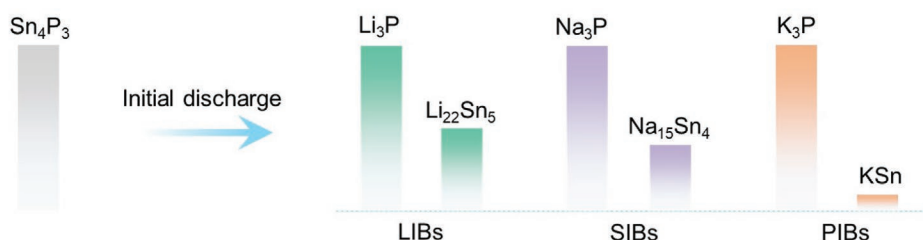
Furthermore, differential electrochemical curves, ex situ XPS, and SEM revealed that the deep intercalation of A$^+$ in P and Sn, especially in P, resulting in the capacity-fading of Sn_4P_3 anode in AIBs. Serious dendrite growth further induces capacity decay in SIBs, while in PIBs it is the unstable solid electrolyte interphase and sluggish dynamics that lead to capacity decay (Scheme 1b,c). Finally, the electrochemical performance of Sn_4P_3 anode is greatly enhanced by the carbon hybridization strategy, which improves the structural stability and dynamics of Sn_4P_3 anode. The understanding of the failure mechanisms, including the structural deterioration, unstable SEI, dendrite growth, and sluggish kinetics, together with the modification strategy and systematic analysis methods used in this study provide theoretical guidance for the development of other alloy-based anode materials.
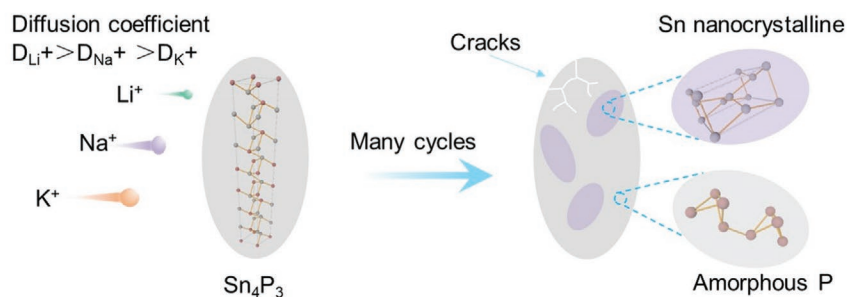
4. Experimental Section

Synthesis of Sn_4P_3 and Sn_4P_3/C: Stoichiometric amounts of Sn powder (Aladdin, 99.999%) and red P (Aladdin, 99.999%) were loaded into a stainless steel jar (50 mL) with a ball (size: 1 mm)-to-powder mass ratio of 100:1. The loading process was conducted in a glove box (MIKROUNA) under an Ar atmosphere with the quantity of H$_2$O and O$_2$ below 0.1 ppm. Thereafter, the jar was clamped to avoid contacting with air. It was then removed from the glove box and installed in a high-energy mechanical milling (HEMM) machine (AM400, Ants Scientific Instruments) at 500 rpm for 3 h. The Sn_4P_3/C composites were also prepared using HEMM under the same conditions, with the prepared Sn_4P_3 samples and Super P as raw materials in a mass ratio of 7:3. All results presented herein were repeated at least three times.

Electrode Preparation: The active materials were mixed with Super P (Super C65, Timcal) and sodium alginate (SA, Aladdin) binder in the mass ratio of 7:2:1 in deionized water. The obtained slurry was then
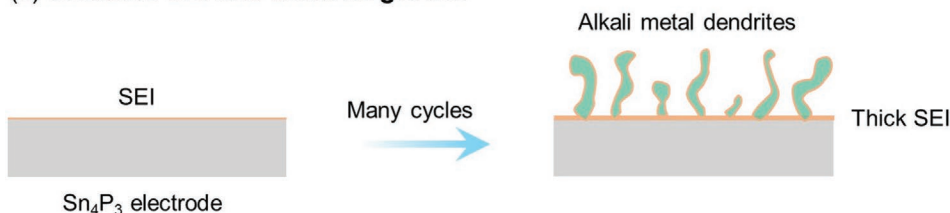
**ADVANCED
SCIENCE NEWS**

www.advancedsciencenews.com

**ADVANCED
FUNCTIONAL
MATERIALS**

www.afm-journal.de

(a) Various final discharge products

(b) Dynamics and structural deterioration

(c) Unstable SEI and dendrite growth

Scheme 1. Schematic of ion storage mechanism and failure theory of Sn_4P_3 anode in AIBs. a) Illustration of various final discharge products of Sn_4P_3 anodes in AIBs. The height of the column for each compound represents its theoretical specific capacity. b) Illustration of the dynamics and structural deterioration of Sn_4P_3 anodes in AIBs. PIBs show sluggish dynamics compared with LIBs and SIBs, resulting from the larger radius of K^+. The Sn_4P_3 anode exhibits obvious phase separation behavior after cycling, i.e., Sn nanocrystalline surrounded by the amorphous P matrix. c) Illustration of the unstable SEI and dendrite growth of Sn_4P_3 anodes in AIBs. The unstable SEI in PIBs and the serious dendrite growth in SIBs further result in capacity-fading of Sn_4P_3 anodes.

cast on the copper current collector at drying temperature of 80 °C. The electrodes were cut into φ14 disks with active material loading of ≈2 mg (thickness of about 35 μm) and further dried at 120 °C prior to battery assembly.

Battery Assembly: Electrochemical tests were conducted in 2032 half coin cells with active materials as the working electrode and glass fiber (Whatman GF/D) as the separator in AIBs. Li, Na, and K metal disks acted as counter electrodes in the LIBs, SIBs, and PIBs respectively, and the thickness of these disks are ≈0.5 mm. $LiPF_6$ (1 м) in an EC-DMC-FEC mixture (4.5/4.5/1 v/v/v), $NaPF_6$ (1 м) in an EC-DMC-FEC mixture (4.5/4.5/1 v/v/v), and KPF_6 (0.8 м) in an EC-DMC-FEC mixture (4.5/4.5/1 v/v/v) acted as electrolytes (the amount of electrolyte in each battery is 80 μL) in the LIBs, SIBs, and PIBs, respectively.

Electrochemical Measurement: Galvanostatic charge-discharge cycles at various C-rates (1 C = 1100 mA g^{-1} for LIBs, 1 C = 600 mA g^{-1} for SIBs, 1 C = 400 mA g^{-1} for PIBs) between 0.005–2 V at 25 °C and the GITT (pulse of 0.1 C for 30 min, with a 3 h interruption between each pulse) were conducted using a CT3001A system (Wuhan LAND). The specific capacity of AIBs are calculated based on the mass of Sn_4P_3 for pure Sn_4P_3 system or Sn_4P_3/C for Sn_4P_3/C composites. CV (voltage range: 0.005–2 V, scan rate: 0.2, 0.5, 1 and 2 mV s^{-1}) and EIS (frequency range: 1 000 000–0.01 Hz,

bias voltage: 0.005 V) were performed using a CHI800D system (CH Instruments). Alkali symmetric batteries with the same alkali metal as the working and counter electrodes were measured at the current density of 0.5 mA cm^{-2} with the capacity limit of 1 mAh cm^{-2}. Alkali metal-Cu batteries were measured with the current density of 0.5 mA cm^{-2} and the capacity limit of 1 mAh cm^{-2} during discharge, and then charged with the current density of 0.5 mA cm^{-2} and the voltage limit of 2 V.

Ex Situ XRD Measurement: 2032 coin batteries were first charged or discharged to the special potential marked in Figure 2a–c, and then disassembled in the glove box to extract the working electrode. After that, the electrode was rinsed with DMC to remove the residual electrolyte, and dried at room temperature. The dried electrode was then fixed on the XRD specimen stage and coated with Kapton tape to protect the sample from air exposure. XRD patterns were recorded using a Bruker D8 Advance diffractometer with a Cu K$_\alpha$ radiation source operating at 40 KV and 40 mA. The test range was 10–80°, the step size was 0.02° and the dwell time was 0.1 s.

Ex Situ SEM Measurement: The dried electrode after disassembling in a glove box was first fixed on an SEM specimen stage, and sealed in a valve bag to protect the sample from air exposure. After that, the sample

was transferred into the SEM sample chamber quickly with a very short exposure time to air (<30 s). SEM and corresponding EDS mapping images were taken using the Hitachi SU8010 SEM operating at 10 KV, 10 mA and 15 KV, 15 mA, respectively.

Ex Situ TEM Measurement: The sample powder was first obtained by scraping the dried electrode in a glove box, and then dispersed in ethyl alcohol. After that, the dispersion was dropped in to a standard Cu grid, and dried at room temperature. TEM images were taken using spherical aberration-corrected FEI Titan Themis Cubed G2 300 TEM operating at 300 KV.

Ex Situ XPS Measurement: The dried electrode after disassembling in the glove box was first fixed on to the XPS specimen stage, and then put in a Vacuum transfer chamber to avoid exposure to moisture. XPS patterns were recorded using a Thermo Fisher Escalab 250Xi XPS with Al K_{α} radiation source. The binding energy was calibrated based on carbon contamination using the C1s peak at 284.8 eV.

Computational Method: DFT calculations were performed using the projector-augmented wave (PAW) potentials[39] and the Perdew–Burke–Ernzerhof (PBE) exchange-correlation functional[40], as implemented in the Vienna Ab-initio Simulation Package.[41] The cut-off of the plane-wave kinetic energies was set to 500 eV. The amorphous Sn_4P_3 structure was simulated using a periodic cubic supercell containing 24 Sn and 18 P atoms. The liquid-quench method was used to create amorphous structures via ab-initio molecular dynamics simulations. The heating temperature was 1000 K. The equations of motion were integrated with the Verlet algorithm using a time step of 1 fs, and the temperature was controlled by the velocity of rescaling and a canonical ensemble (NVT) using a Nosé–Hoover thermostat. Similar calculation schemes have been employed successfully in previous studies.[42,43] The formation energy of $A_xSn_4P_3$ is defined as:

$$E_f(x) = E(A_xSn_4P_3) - E(Sn_4P_3) - x \cdot E(A) \tag{1}$$

where $E(A_xSn_4P_3)$, $E(Sn_4P_3)$, and $E(A)$ are the total energies of $A_xSn_4P_3$, Sn_4P_3, and bulk (bcc) A, respectively. The specific capacity C (mAh g^{-1}) is calculated using the following equation:

$$C = \frac{x \times n \times F \times 10^3}{M} \tag{2}$$

where n is the valence number of A, F is the Faraday constant at 26.8 Ah mol^{-1}, and M is the molecular mass of Sn_4P_3. The average voltage V is calculated as follows:

$$V(x) = \frac{E(A_{x1}Sn_4P_3) - E(A_{x2}Sn_4P_3) + (x2 - x1)E(A)}{(x2 - x1)} \tag{3}$$

where $E(A_{x1}Sn_4P_3)$, $E(A_{x2}Sn_4P_3)$, and $E(A)$ are the total energies of the $A_{x1}Sn_4P_3$, $A_{x2}Sn_4P_3$, and Im3m alkali metals, respectively.

Supporting Information

Supporting Information is available from the Wiley Online Library or from the author.

Conflict of Interest

The authors declare no conflict of interest.

Data Availability Statement

Research data are not shared.

[1] J.-M. Tarascon, M. Armand, *Nature* **2001**, *414*, 359.
[2] J. B. Goodenough, Y. Kim, *Chem. Mater.* **2010**, *22*, 587.
[3] J. Zhou, Q. Shi, S. Ullah, X. Yang, A. Bachmatiuk, R. Yang, M. H. Rummeli, *Adv. Funct. Mater.* **2020**, *30*, 2004648.
[4] M. Armand, J. M. Tarascon, *Nature* **2008**, *451*, 652.
[5] D. Larcher, J. M. Tarascon, *Nat. Chem.* **2015**, *7*, 19.
[6] C. Vaalma, D. Buchholz, M. Weil, S. Passerini, *Nat. Rev. Mater.* **2018**, *3*, 18013.
[7] W. Zhang, Y. Liu, Z. Guo, *Sci. Adv.* **2019**, *5*, eaav7412.
[8] N. Yabuuchi, K. Kubota, M. Dahbi, S. Komaba, *Chem. Rev.* **2014**, *114*, 11636.
[9] T. Hosaka, K. Kubota, A. S. Hameed, S. Komaba, *Chem. Rev.* **2020**, *120*, 6358.
[10] Z. P. Cano, D. Banham, S. Ye, A. Hintennach, J. Lu, M. Fowler, Z. Chen, *Nat. Energy* **2018**, *3*, 279.
[11] A. Kwade, W. Haselrieder, R. Leithoff, A. Modlinger, F. Dietrich, K. Droeder, *Nat. Energy* **2018**, *3*, 290.
[12] J. W. Choi, D. Aurbach, *Nat. Rev. Mater.* **2016**, *1*, 16013.
[13] Y. Li, Y. Lu, P. Adelhelm, M. M. Titirici, Y. S. Hu, *Chem. Soc. Rev.* **2019**, *48*, 4655.
[14] E. Irisarri, A. Ponrouch, M. R. Palacin, *J. Electrochem. Soc.* **2015**, *162*, A2476.
[15] J. Ni, L. Li, J. Lu, *ACS Energy Lett.* **2018**, *3*, 1137.
[16] Y. Sun, L. Wang, Y. Li, Y. Li, H. R. Lee, A. Pei, X. He, Y. Cui, *Joule* **2019**, *3*, 1080.
[17] Z. Zhou, Z. Jiang, S. Niu, S. Zhu, J. Zhou, Y. Zhu, J. Liang, D. Han, K. Xu, L. Zhu, X. Liu, G. Wang, Y. Qian, *Chem* **2018**, *4*, 372.
[18] W. Li, X. Li, J. Liao, B. Zhao, L. Zhang, L. Huang, G. Liu, Z. Guo, M. Liu, *Energy Environ. Sci.* **2019**, *12*, 2286.
[19] N. Yabuuchi, Y. Matsuura, T. Ishikawa, S. Kuze, J.-Y. Son, Y.-T. Cui, H. Oji, S. Komaba, *ChemElectroChem* **2014**, *1*, 580.
[20] H. Jin, S. Xin, C. Chuang, W. Li, H. Wang, J. Zhu, H. Xie, T. Zhang, Y. Wan, Z. Qi, W. Yan, Y.-R. Lu, T.-S. Chan, X. Wu, J. B. Goodenough, H. Ji, X. Duan, *Science* **2020**, *370*, 192.

[21] J. Zhou, X. Liu, L. Zhu, S. Niu, J. Cai, X. Zheng, J. Ye, Y. Lin, L. Zheng, Z. Zhu, D. Sun, Z. Lu, Y. Zang, Y. Wu, J. Xiao, Q. Liu, Y. Zhu, G. Wang, Y. Qian, *Chem* **2020**, *6*, 221.

[22] X. Fan, J. Mao, Y. Zhu, C. Luo, L. Suo, T. Gao, F. Han, S.-C. Liou, C. Wang, *Adv. Energy Mater.* **2015**, *5*, 1500174.

[23] M. Winter, J. r. O. Besenhard, *Electrochim. Acta* **1999**, *45*, 31.

[24] Y. Idota, *Science* **1997**, *276*, 1395.

[25] W. Zhang, W. K. Pang, V. Sencadas, Z. Guo, *Joule* **2018**, *2*, 1534.

[26] J. Qian, Y. Xiong, Y. Cao, X. Ai, H. Yang, *Nano Lett.* **2014**, *14*, 1865.

[27] Y. Xu, B. Peng, F. M. Mulder, *Adv. Energy Mater.* **2018**, *8*, 1701847.

[28] W. Zhang, J. Mao, S. Li, Z. Chen, Z. Guo, *J. Am. Chem. Soc.* **2017**, *139*, 3319.

[29] S. C. Jung, Y.-K. Han, *J. Phys. Chem. C* **2015**, *119*, 12130.

[30] S. C. Jung, J.-H. Choi, Y.-K. Han, *J. Mater. Chem. A* **2018**, *6*, 1772.

[31] J. Sun, H. W. Lee, M. Pasta, H. Yuan, G. Zheng, Y. Sun, Y. Li, Y. Cui, *Nat. Nanotechnol.* **2015**, *10*, 980.

[32] C. M. Park, H. J. Sohn, *Adv. Mater.* **2007**, *19*, 2465.

[33] S. Jiao, X. Ren, R. Cao, M. H. Engelhard, Y. Liu, D. Hu, D. Mei, J. Zheng, W. Zhao, Q. Li, N. Liu, B. D. Adams, C. Ma, J. Liu, J.-G. Zhang, W. Xu, *Nat. Energy* **2018**, *3*, 739.

[34] P. Verma, P. Maire, P. Novák, *Electrochim. Acta* **2010**, *55*, 6332.

[35] K. N. Wood, G. Teeter, *ACS Appl. Energy Mater.* **2018**, *1*, 4493.

[36] P. M. L. Le, T. D. Vo, H. Pan, Y. Jin, Y. He, X. Cao, H. V. Nguyen, M. H. Engelhard, C. Wang, J. Xiao, J. G. Zhang, *Adv. Funct. Mater.* **2020**, *30*, 2001151.

[37] A. J. Naylor, M. Carboni, M. Valvo, R. Younesi, *ACS Appl. Mater. Interfaces* **2019**, *11*, 45636.

[38] T. Brezesinski, J. Wang, S. H. Tolbert, B. Dunn, *Nat. Mater.* **2010**, *9*, 146.

[39] P. E. Blochl, *Phys. Rev. B: Condens. Matter Mater. Phys.* **1994**, *50*, 17953.

[40] J. P. Perdew, K. Burke, M. Ernzerhof, *Phys. Rev. Lett.* **1996**, *77*, 3865.

[41] G. Kresse, J. Furthmüller, *Phys. Rev. B* **1996**, *54*, 11169.

[42] S. C. Jung, H. J. Kim, J. W. Choi, Y. K. Han, *Nano Lett.* **2014**, *14*, 6559.

[43] S. C. Jung, Y.-K. Han, *J. Phys. Chem. Lett.* **2013**, *4*, 2681.